Numerical and Experimental Investigation of Early Stage Diesel Sprays

M. Ghiji[a,*], L. Goldsworthy[a], P.A. Brandner[a], V. Garaniya[a], P. Hield[b]

[a] Australian Maritime College, University of Tasmania, Launceston, Tasmania, Australia

[b] Defence Science and Technology Group, Melbourne, Victoria, Australia

Abstract

Experimental and numerical investigations of primary atomization in a high-pressure diesel jet are presented. Information on flow processes and structures inside and near nozzle exit are described at early and quasi-steady stages of injection. The numerical method is based on the Volume Of Fluid (VOF) phase-fraction interface capturing technique, in an Eulerian framework. The influence of grid resolution, convection interpolation scheme and temporal integration scheme on the modelling of jet physics are investigated. The present flow setup includes in-nozzle disturbances with the no-slip condition at the walls. All experimental operating conditions are replicated in the numerical models. The early stage liquid jet leading edge demonstrates an umbrella-shaped structure in the numerical results which is in qualitative agreement with experimental imaging. Data obtained provide insight into the flow behavior in the dense region including commencement of fragmentation and early spray angle formation. Experimental images show a cloud of air-fuel mixture at the early stage of injection. The existence of ingested air inside the injector after needle closure could be the source of the observed deviation between experimental and numerical results. The results show that the jet break-up rate and liquid core length increase in cases with higher grid resolutions. The early spray angle from the numerical results at the quasi-steady stage, shows good agreement with experimental data.

Keywords

High-pressure diesel spray; Primary atomization; Near-nozzle flow; In-nozzle turbulence; Large Eddy Simulation; Eulerian/VOF.

*Corresponding author. Tel.:+61 3 6324 9840
 Email address: mghiji@utas.edu.au (M. Ghiji)

1. Introduction

Steady and unsteady liquid jet flows and their breakup remain an ongoing field of investigation [1-8]. Jets are of broad interest for the study of many basic phenomena and in a range of physical processes. They occur at length scales ranging from the order of atomic to that of the universe. In many applications, they may be multi-phase and involve multiple phase changes, chemical reactions and complex flow phenomena.

Human impacts on the environment and more specifically global warming are increasing government concerns on strict emission standards for engine manufacturers. The quality of air-fuel mixing is mainly driven by atomization of the injected liquid jet, which plays an important role in the combustion process, ultimately controlling production of pollutants. Engine manufacturers are constantly aiming to reduce exhaust gas emissions by optimizing the fuel injection process. A wide range of engine operating conditions makes the optimization of air-fuel mixing difficult [8-11]. The motivation, on one hand, is practical applications such as manufacturing of diesel engine injectors and, on the other hand, understanding the origin of key phenomena of atomization and its influence on jet breakup processes.

In diesel engines, combustion chambers are fed by high-pressure fuel injected as a solid cone spray. This spray undergoes a series of instabilities (longitudinal and transverse) which lead to the fragmentation of the liquid bulk into structures that further disintegrate into droplets. This initial process of atomization is called primary breakup and occurs in the vicinity of the injection point. Primary breakup mechanisms initiate the atomization process, control the extent of the liquid core and provide initial conditions for secondary breakup in the disperse flow region [5, 10, 12, 13].

Despite the fact that atomization is widely utilized and significantly affects engine combustion processes, heat release rate and exhaust emissions [2, 14-17], the characteristics of the spray produced

(for example size and velocity distributions of droplets) are still not well predicted due to the small length and time scales and high liquid fractions involved, especially inside the jet.

So far, many theories have been proposed to describe the primary atomization mechanism, including: aerodynamic shear forces which act through stripping and Kelvin-Helmholtz (K-H) instabilities [8, 18, 19]. Turbulence-induced disintegration has a significant effect on jet breakup at higher Reynolds numbers $Re_l = \rho_l\, U\, D\, /\, \mu_l$, where ρ_l is the liquid density, U is the liquid velocity, D is the orifice diameter, and μ_l is the dynamic viscosity [14, 16, 20-23]. Relaxation of the velocity profile, creates a bursting effect especially in non-cavitating jets and large velocity differentials [24]. Cavitation-induces disintegration of the jet due to the reduction of cross-sectional area at the nozzle inlet [25-28]; and liquid bulk oscillation provoking toroidal surface perturbations [8, 29].

Less of a consensus has been achieved in determining the dominant mechanisms of early breakup when a high-speed liquid jet is injected into a pressurized dense gas. Many interdependent phenomena can provoke severe velocity fluctuations leading to a nonlinear instability of the flow inside the nozzle. These phenomena include turbulence [16, 20-23] generated by the nozzle geometry and by the collapse of cavitating bubbles [25-28]. In addition to turbulence, fluctuations of the injection velocity [24] and drop shedding [14, 30] contribute to the primary breakup. Experimentally separating and investigating these different effects is very difficult. For the development of diesel engines with both optimal fuel economy and minimum pollutant emissions, it is necessary to comprehend the spray processes and then characterize the effects of different parameters and engine operating condition on fuel flow structures. This is a challenging subject to study, both experimentally and numerically [4, 15, 18, 31, 32]. In this study, the flow inside the nozzle and the liquid bulk near the nozzle exit and its fragmentation (primary atomization) are investigated.

68 This paper concentrates on the effect of in-nozzle turbulence. The effects of cavitation will be studied

69 in future work. Turbulent flows are represented by eddies with an entire range of length and time scales.

70 Large eddy simulation (LES) directly resolves large scale eddies and models small eddies. Simulating

71 only small eddies and solving the large eddies allows the use of much coarser meshes and longer time

72 steps in LES compared to Direct Numerical Simulation (DNS). Despite this, LES still needs principally

73 finer meshes compared to the ones used for Reynolds Averaged Navier Stokes (RANS) computations.

74 Since RANS models cannot capture the transient spray structure [5, 6, 8, 9] including droplet clustering

75 and shot to shot variability, LES is applied to overcome these limitations.

76 Literature reviews of the existing atomization models, demonstrated that all these models (blob,

77 Huh/Gosman, MPI, Arcoumanis, Nishimura, V.Berg, Baumgarten, ReitzWave model, Taylor Analogy

78 Breakup model) [9, 32, 33] simplify droplet generation in the dense region (primary atomization) which

79 might make the simulation inaccurate and unrealistic [6, 18]. For example, the blob model as the most

80 employed model not only simply generates parcels with the size of the nozzle diameter but also does not

81 take into account the physics of in-nozzle turbulence and in-nozzle cavitation. In addition, these

82 conventional atomization models with Lagrangian Particle Tracking (LPT), limit the grid fineness near

83 the nozzle and do not allow LES to capture the features of the spray and background fluid flow near the

84 nozzle. Furthermore, refining the grid with the blob method results in problems with high liquid fraction

85 in the LPT approach (too much liquid in each cell) [5, 6, 9, 34]. These limitations motivate the use of the

86 Eulerian approach to model the primary atomization, instead of using conventional atomization models.

87 With ever increasing computational power, there is an incentive to use more complex models for primary

88 atomization. This is a key aim of the present work.

89 To date, considerable progress has been made in the development of rigorous numerical methods for

90 performing highly resolved simulations of multiphase flow [8, 35]. The accuracy of different numerical

91 techniques for modelling the primary atomization of a liquid diesel jet was investigated in detail for low

Re (Re < 5000) by Herrmann [20] and Desjardins & Pitsch [36]. Herrmann [20], demonstrated the importance of the grid resolution on capturing the accurate phase interface geometry of diesel liquid with an injection velocity of $100 \, \mathrm{m/s}$ and Re = 5000. Turbulence was reported as the dominant driving mechanism of atomization within the first 20 nozzle diameters downstream.

Due to the lack of detailed studies of the primary atomization of diesel liquid jets under real diesel engine operating conditions, the present study focuses on the structure of primary atomization with an accelerating injection pressure up to 1200 bar, background pressure of 30 bar, liquid Reynolds number within the range $7000 \leq Re_l \leq 37000$, and liquid Weber number of $We_l \approx 933843$ at quasi-steady stage. The liquid Weber number $We_l = \rho_l \, U_p \, d \, / \, \sigma$, where U_p is the droplet relative velocity, d is the droplet diameter and σ is the surface tension. The Reynolds number is calculated based on average liquid velocity at the nozzle hole exit. The large range of Re is due to rising pressure at the sac inlet, changing from 30 bar at the beginning of injection up to 1200 bar at the quasi-steady stage of injection. In-nozzle cavitation is not considered in this work however this constraint will be eliminated in further studies. The present work focuses on the very early stages of injection as it is likely that instabilities generated in the early stages have significant effect on the development of the whole spray. Non-evaporating conditions are employed to simplify the physical complexities.

## 2. Methodology

2.1 Experimental apparatus

Non-evaporating diesel fuel spray measurements were conducted with a laser based imaging system in a constant volume High-Pressure Spray Chamber (HPSC). The HPSC operating volume is a square-section prism with rounded corners and the axis vertically oriented. Optical access to the injection test chamber is via three windows in the test chamber walls 80 mm thick, UV quality, optically polished

114 quartz, and viewing area of 200×70 mm. The light source is a 120 milliJoule dual-cavity Nd:YAG laser

115 capable of light pulses around 5 ns duration.

116 The chamber is pressurized to 30 bar with temperature and density of 298 K and 35 kg/m³,

117 respectively, to give air density in the range of a heavy duty diesel engine. Diesel fuel is axially injected

118 through a single solid cone fuel nozzle with an injection pressure of around 1200 bar from the top of the

119 HPSC as shown in Figure 1.
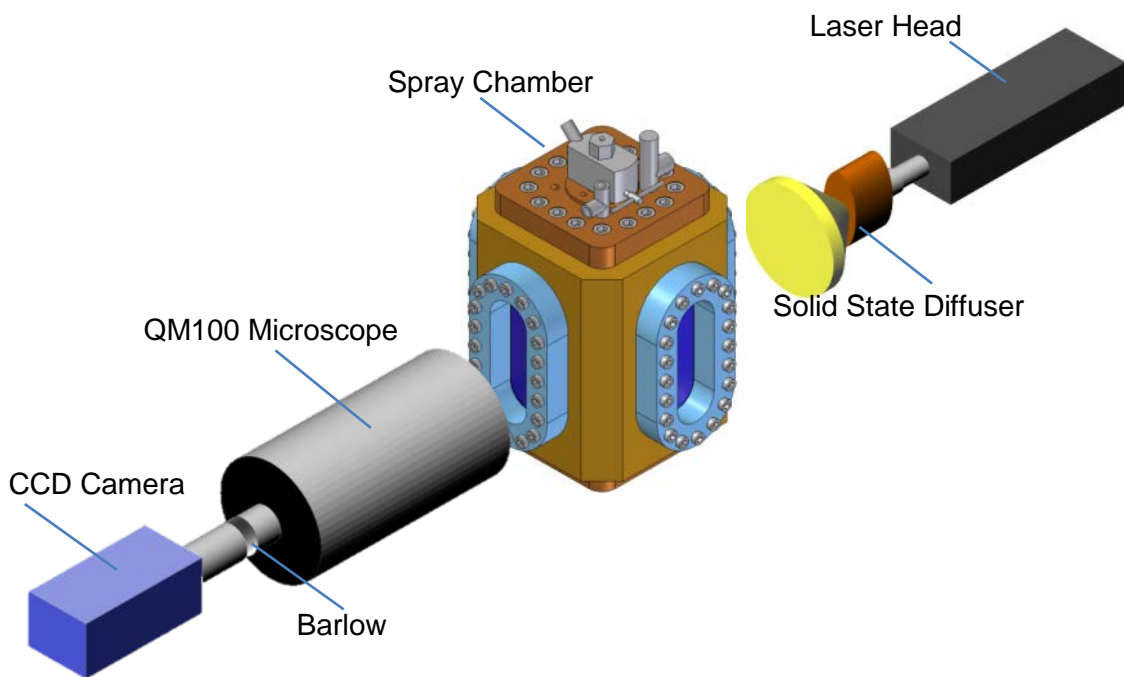
120

121 **Figure 1.** Schematic view of the High-Pressure Spray Chamber showing laser and camera setup for
122 shadowgraphy measurements.

123 The injection pressure profile which is highly repeatable from shot to shot is replicated based on the

124 previous study of Bong et al [9]. The injector needle valve snaps open when the injector pressure achieves

125 a given value, as determined by the tension of the needle valve spring. Needle lift is monitored using an

126 eddy current proximity probe. It takes about 0.2 ms for the needle valve to lift completely.

127   The acquisition sequence is triggered by a pulse from the injector driver and the delay to the start of

128   image acquisition is measured separately. The needle lift signal and the pulse generated by the laser were

129   recorded using a digital oscilloscope to record the time at which the laser light pulse is activated, as

130   indicated by the Q-switch pulse. Using shots obtained at the point where the spray is just starting to

131   emerge from the nozzle, it is established that there is a delay of $100 \pm 5\,\mu s$ between start of injection and

132   a significant response from the needle lift transducer. This information enables timing of subsequent

133   shots.

134   A laser-based backlit imaging method (shadowgraphy) is used to investigate the micro-spray

135   structure. As depicted in Figure 1, a Questar QM100 long distance microscope is attached to a LaVision

136   Imager Intense dual-frame, 12 bit CCD camera with 1376×1040 pixels. The camera and laser allow only

137   two images to be taken for each shot of the injector. The delay between the two images can be as low as

138    $0.5\,\mu s$. The use of closely spaced images allows estimation of the propagation velocity of the leading

139   edge of the injected fuel. An interval of about 30 s is allowed between injector shots to allow the chamber

140   to settle.

141   The spray is backlit with laser light through a standard solid-state diffuser supplied by LaVision. The

142   diffuser employs laser-induced fluorescent from an opaque plate impregnated with a fluorescent dye. The

143   camera is focused, aligned, and calibrated on a graduated scale on the spray axis.

144   Two sets of microscopic data are achieved with and without using a Barlow lens. With the 2x Barlow

145   lens, mounted between CCD Camera and Microscope, a magnification of 7.7:1, a field of view of

146    $1157 \times 860\,\mu m$ and a spatial resolution of $0.84\,\mu m/pixel$ are achieved. These sets of data are used as a

147   benchmark to validate the numerical results close to the nozzle exit.

2.2   Simulation setup

2.2.1   Mathematical method

150   In this study, the VOF phase-fraction based interface capturing technique similar to de Villiers et al

151   [11] is employed in the open source numerical code OpenFOAM v2.3. The code considers the two-phase

152   flow field as a single incompressible continuum with constant density ρ and viscosity μ, including surface

153   tension. The compressibility effect will be included in future studies. The basic form of the governing

154   mass and momentum conservation are:

$$\nabla.\boldsymbol{V} = 0 \tag{1}$$

$$\frac{\partial \rho \boldsymbol{V}}{\partial t} + \nabla.(\rho \boldsymbol{V}\boldsymbol{V}) = -\nabla p + \nabla.\tau + \int_{S(t)} \sigma k' \boldsymbol{n}' \delta(x - x') dS \tag{2}$$

155   Where $\boldsymbol{V}$ is the velocity, $\boldsymbol{p}$ is the pressure, $\boldsymbol{t}$ is the time, $\boldsymbol{\tau}$ is the stress tensor, $\boldsymbol{\kappa}$ is the local curvature

156   of the liquid surface and, $\boldsymbol{n}$ denotes a unit vector normal to the liquid surface $\boldsymbol{S}$. The operators $\nabla()$ and

157    $\nabla.()$ represent the gradient and the divergence operations, respectively. The integral term in equation (2)

158   represents the momentum source due to surface tension force on the interface $\boldsymbol{S(t)}$. This force only acts on

159    $\boldsymbol{S}$, as ensured by the indicator function $\boldsymbol{\delta(\ldots)}$. The time-varying phases interface $\boldsymbol{S(t)}$ is located

160   accordingly using a VOF surface-capturing approach which utilizes the volume fraction $\boldsymbol{\gamma}$ of diesel fuel as

161   an indicator function, defined as:

$$\gamma = \begin{cases} 1 & \text{for a point inside the liquid} \\ 0 < \gamma < 1 & \text{for a point in the transitional region} \\ 0 & \text{for a point inside the air} \end{cases} \tag{3}$$

162   The 'transitional region', where the interface is located, utilized as an artefact of the numerical

163   solution process. Fluid in a transition region is considered as a mixture of the two fluids on each side of

164   the interface, which cannot completely resolve a discontinuous step. The transport equation for the

165   indicator function is:

$$\frac{\partial \gamma}{\partial t} + \nabla.(V\gamma) = 0 \tag{4}$$

166   According to the definitions of γ, the local thermo-physical properties are given by:

$$\rho = \gamma\rho_l + (1-\gamma)\rho_g \tag{5}$$

$$\mu = \gamma\mu_l + (1-\gamma)\mu_g \tag{6}$$

167   where the subscripts l and g represents the liquid and gas, phases respectively.

168   The LES/VOF equations are derived from equations (1), (2) and (4) using localized volume

169   averaging of the phase-weighted hydrodynamics variables. This process known as filtering, includes

170   decomposition of the relevant variables into resolvable and sub-grid scales of turbulent fluctuations. As

171   the results of the filtering process, the sub-grid scale fluctuations will be eliminated from direct

172   simulation. This filtering together with the non-linear convection terms in equation (2) introduce an

173   additional quantity, comprising correlation of the variable fluctuations at sub-grid scales that entail

174   closure through mathematical models, known as the subgrid scale (SGS) stresses $\boldsymbol{\tau}^{\mathbf{sgs}}$ as they signify the

175   influence of the unresolved small scales of turbulence, given by:

$$\tau^{sgs} = \overline{VV} - \overline{V}\ \overline{V} \tag{7}$$

176   and estimated by a single subgrid scale model of the eddy-viscosity type:

$$\tau^{sgs} - \frac{2}{3}\ k\ \boldsymbol{I} = -\ \frac{\mu^{sgs}}{\rho}\ (\nabla\overline{\boldsymbol{V}} +\ \nabla\overline{\boldsymbol{V}}^T) \tag{8}$$

177   where $\boldsymbol{k}$ is the subgrid scale turbulent energy and $\boldsymbol{\mu}^{sgs}$ is the subgrid scale viscosity, both are determined

178   from the one-equation SGS turbulent energy transport model accredited to Yoshizawa [37].

$$\frac{\partial k}{\partial t} + \nabla.(k\bar{V}) = \nabla.[(v + v^{sgs})\nabla k + \tau^{sgs} \cdot \bar{V}] - \varepsilon - \frac{1}{2}\tau^{sgs} : (\nabla\bar{V} + \nabla\bar{V}^T) \tag{9}$$

179   where $\varepsilon = C_\varepsilon k^{2/3}/\Delta$ is the SGS turbulent dissipation rate, $\boldsymbol{v}^{sgs} = C_k k^{1/2}/\Delta$ and $\Delta = \sqrt[3]{V}$ is the SGS

180   length scale where V is volume of the computational cell. The coefficients, found from statistical

181   considerations, are $C_k = 0.05$ and $C_\varepsilon = 1$ [6].

2.2.2   The Numerical solution method

183   Mathematical models for this simulation are solved using an implicit finite-volume method, which

184   employs spatial and temporal discretization schemes. This method preserves a sharp interface resolution

185   by including a compression velocity term [38] in the phase transport equation, acting to compress the

186   VOF interface. The solution procedure utilizes the Pressure Implicit with Split Operator (PISO) algorithm

187   [39], together with conjugate gradient methods for coupled solution of mass and momentum conservation

188   equations which is specifically suited to transient flows [40].

189   In order to preserve the proper physical limits on the fluid-dynamics variables, different integration

190   schemes are tried from highly dissipative up to highly conservative. In this study, the advection terms are

191   solved by the Normalized Variable (NV) Gamma differencing scheme [41]. A conservative, bounded,

192   second-order scheme is used for Laplacian derivative terms and a second-order, implicit discretization

193   scheme is used for time derivative terms. The numerical integration time-step is adjusted by various

194   stability criteria, and is of the order 1×10^{-9} s for the fine case.

2.2.3   Boundary conditions and initial setup

196   Atomization is affected by the design of the sac and nozzle orifice inlet which consequently influence

197   primary breakup [8, 14, 18]. The computational domain has therefore been modelled using the geometry

198   of the experimental nozzle determined using X-ray Computer Aided Tomography (CAT) analysis as

199   shown in Figure 2. This analysis reconstructs the images with pixel numbers of $1016 \times 1024 \times 1024$, and

200   effective voxel size of 2.318 µm.

201
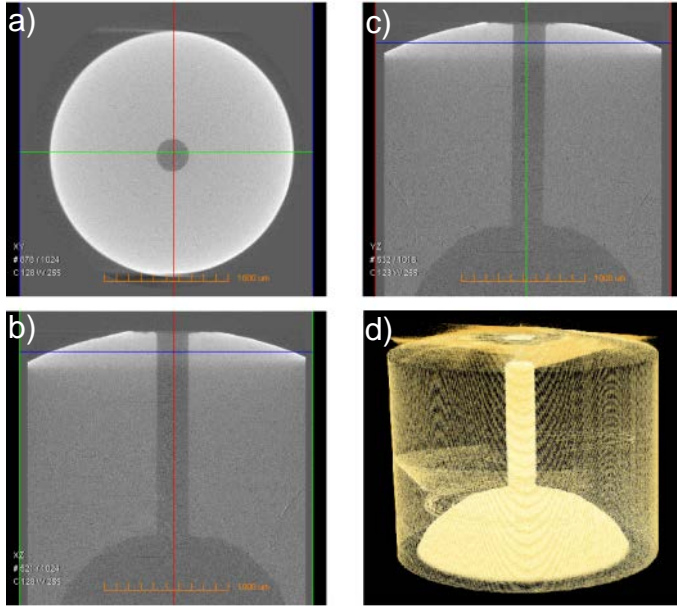
Figure 2. X-Ray Tomography measurement of sac and nozzle geometry and dimensions. a) X-Y view; b) X-Z view; c) Y-Z view and d) 3D view of nozzle. Images provided by The Centre for Materials and Surface Science and the Centre of Excellence for Coherent X-ray Science at La Trobe University, employing an Xradia MicroXCT instrument.

All the experimental conditions were replicated in numerical models including the sac volume inlet, spray chamber pressure and air and diesel fuel temperature and viscosity. Fuel properties and set up conditions are listed in Table 1. The sac inlet pressure is ramped from 30 bar initially to 850 bar after 50 µs then to 1200 bar after a further 25 µs then constant at 1200 bar to the end of simulation. This is to some extent arbitrary but is premised on published data implying that the sac pressure rises rapidly during needle opening [1, 42-44]. For instance, Moon et al. [1] found that quasi-steady stage jet velocity was reached when the needle lift was only 17% of the maximum needle lift. The ramp was chosen to give an approximate match of modelled and experimental penetration rates. The lower pressure rise rate in the second 25 µs was adopted to avoid numerical instabilities.

In the present study, it was found that the duration of the needle lift is about 200 µs and that the signal from the eddy current needle lift transducer signal has a delay of around 100±5 µs compared to actual needle lift. This is determined by observing the timing of the laser Q-switch signal relative to the

needle lift signal for shots where the captured image shows the spray just starting to emerge from the nozzle. Thus, the needle lift signal could not be used to determine instantaneous needle position. The maximum needle lift is about 200 µm.

Table 1. Fuel properties and operating conditions based on experimental setup [45]. * Injection velocity, Weber and Mach numbers are for the quasi-steady stage of spray [45]. The nozzle diameter is used as the length scale.

Parameter	Value
Injection pressure	120 MPa average
Nozzle diameter	0.25 mm
Nozzle length	1.6 mm
Nozzle nominal geometry	$K_S = 0$
Fuel	Diesel
Diesel fuel density	832 kg/m^3
Gas	Compressed air
Density ratio	42
Fuel Kinematic viscosity	2.52×10^{-6} m^2/s
Surface tension	0.03 N/m
Temperature	25°C
Fuel Re_l	$7000 \leq Re \leq 37000$
*Indicative injection velocity	367
*Fuel Mach number	367 / 1250 = 0.3
*We_l	933843
*Ohnesorge number	0.077
Chamber pressure	30 bar

The nozzle orifice at the start of each injection in the experimental injections is not necessarily full of fuel due to needle bounce and dribble phenomena at closure nor empty of fuel due to cohesive and adhesive forces. Hence for a good comparison of modelled and measured injection, a method for determining the position of the liquid-gas interface in the nozzle orifice at the start of injection was implemented. Firstly, the sac and three quarters of the nozzle were filled with diesel fuel at a pressure of 30 bar and then the sac inlet pressure raised as described above. Later on, at the end of the injection cycle when the needle closes, the boundary condition is changed from inlet to wall to prevent any further fuel entering the sac, emulating the needle valve closure process. The result of this simulation is that the

232 nozzle fills with liquid to 5.2 D (81% of the nozzle length) from the nozzle entrance. This is due to the

233 equilibrium between adhesive forces, surface tension of the liquid phase and hydrodynamic forces

234 amongst liquid and pressurized air in the spray chamber. The position of the liquid-gas interface inside

235 the nozzle orifice resulting from this simulation (at 5.2 D) is used to initialize the main simulation. This

236 starting point is somewhat arbitrary but goes some way to accounting for air ingestion as described in

237 [42-44, 46].

238 Considering the boundary layer, atomization zone and no-slip condition at the walls (sac and orifice),

239 a hexahedral structured mesh was generated as shown in Figure 3. It has been reported that the spray

240 structure is not axisymmetric [5, 9, 14, 34, 45], therefore the full computational domain (360°) of the

241 atomization zone is meshed.

242
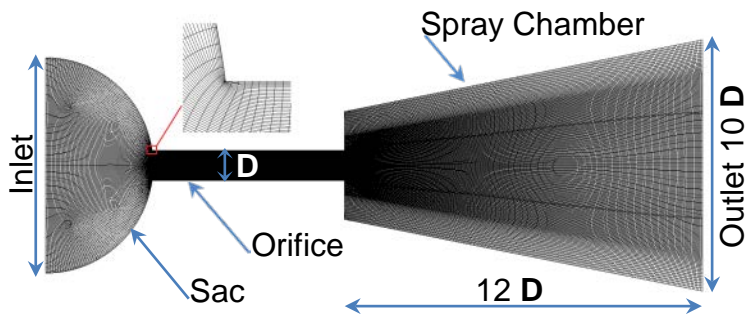
Figure 3. Computational domain and boundary conditions (coarse case, with refined mesh in the orifice and atomization regions).

243 In order to conduct a mesh sensitivity study, three different mesh resolutions are generated with

244 coarse (4 million cells), medium (8 million cells), and fine grids (20 million cells). Cell size is refined

245 down to 0.1 µm in the orifice and 1.7 µm in the primary atomization zone in the finest resolution case.

246 This cell size can capture droplets down to the 10 µm range based the optimistic premise that 5 cells can

247 give reasonable representation of a single droplet [20]. The resolution of these cases, time-step range,

248 number of CPUs, and computational cost (wall clock time) for each case are summarized in Table 2.

249 **Table 2.** Summary of mesh parameters for numerical models

Case	Average Resolution (μm)			Cell count	Time Step ($\times 10^{-9}$ S)	CPU (core count)	Wall clock time (hours)
	Sac	Orifice	Spray Chamber				
Coarse	13	2	6.5	4×10^6	$1.6 \leq \Delta T \leq 80$	128	151.4
Medium	7.5	1.2	5	8×10^6	$1.2 \leq \Delta T \leq 60$	256	225.8
Fine	4	0.5	3.5	20×10^6	$0.9 \leq \Delta T \leq 30$	384	565.3

250   Being aware of the importance of in-nozzle generated turbulence on primary atomization [18, 20], in

251   the fine case, special consideration was given to generating the mesh inside the nozzle orifice. The size of

252   cells in the orifice were decreased to the order of the Kolmogorov length scale for the liquid phase, $\boldsymbol{\eta_l}$, to

253   assure that the smallest generated eddies, as a result of boundary layer and change in cross sectional area,

254   are well resolved. The smallest length scales associated with the flow field for the quasi-steady stage of

255   spray are reported in Table 3. It can be seen in this table that $\boldsymbol{\eta_l}$ is much larger than mesh size in the

256   nozzle for the finest grid. To resolve a given length scale it is necessary that $\eta_l \geq 2\Delta x$, where Δx is the

257   grid size [41]. This mesh resolution leads to the proper prediction of small eddies of the liquid phase

258   inside the nozzle orifice in the fine resolution case. A sub-grid scale model is needed for the turbulence in

259   the gas phase.

260   **Table 3.** Kolmogorov length scales for the liquid and gas phases of the quasi-steady stage of spray where

261   the turbulence intensities used are 4.4 % and 10 %, respectively.

Parameter	Value
Liquid phase Kolmogorov length scale, η_{liq}	0.7 μm
Minimum mesh size in nozzle hole for fine case, Δx_{min}	0.1 μm
Gas phase Kolmogorov length scale, η_{gas}	0.008 μm
Minimum mesh size in spray chamber for fine case, Δx_{min}	1.7 μm

262   **2.2.4 Mesh sensitivities**

263   In this research structured grids are used to achieve higher quality and control which may be

264   sacrificed in unstructured and hybrid meshes. In addition, the efficiency of the differencing scheme for

265 bounding the convection term of the transport equations in a structured mesh is much higher in

266 comparison to an unstructured mesh [47].

267 It is possible that the present conically stretched grid leads to greater spray angle than a purely

268 Cartesian/orthogonal grid, for example. The core of the mesh is purely Cartesian/orthogonal, and the

269 divergence immediately adjacent to the core region is less than near the outer boundaries. Using a

270 structured mesh as in the present study reduces the effects of divergence from orthogonality. A non-

271 orthogonality corrector is employed in the numerical solution to minimize any possible grid orientation

272 influences.

3. Results and discussions

274 Due to the unavailability of a transparent orifice, only images of the spray in the chamber are

275 presented. The comparisons between simulations and experiments are qualitative and focus on the overall

276 spray shape, surface irregularities, spray penetration and generated droplets. The numerical data presented

277 in the next two sections are obtained by means of the second-order time derivatives method and the NV

278 Gamma scheme for solving the convection terms.

3.1 In-nozzle turbulence

280 Figure 4 illustrates the influence of mesh resolution on turbulent eddies, generated and developed

281 within the orifice boundary layer leading to small/large-scale irregularities. These irregularities are the

282 origin of jet surface instabilities. This Figure shows a zoomed view of the jet turbulent structures inside

283 the nozzle orifice demonstrating the small-scale eddies in each case at the quasi-steady stage (sac inlet

284 pressure of 1200 bar and Re of 37000 at the orifice exit). In the left column (images a, c, and e), in-nozzle

285 flow is coloured by velocity magnitude. In the right column at corresponding times (images b, d, and f),

286 the turbulent eddies are depicted using a Q-criterion isosurface of 5×10^9, coloured by static pressure.

287 Negative static pressures after the nozzle entrance are due to the absence of a cavitation model. In the

288   high-resolution case, smaller eddies have been resolved demonstrating the importance of mesh resolution

289   on predicting upstream flow conditions.

Velocity (m/s)

0   600

Static Pressure (Pa)

-1e8   5e7

290
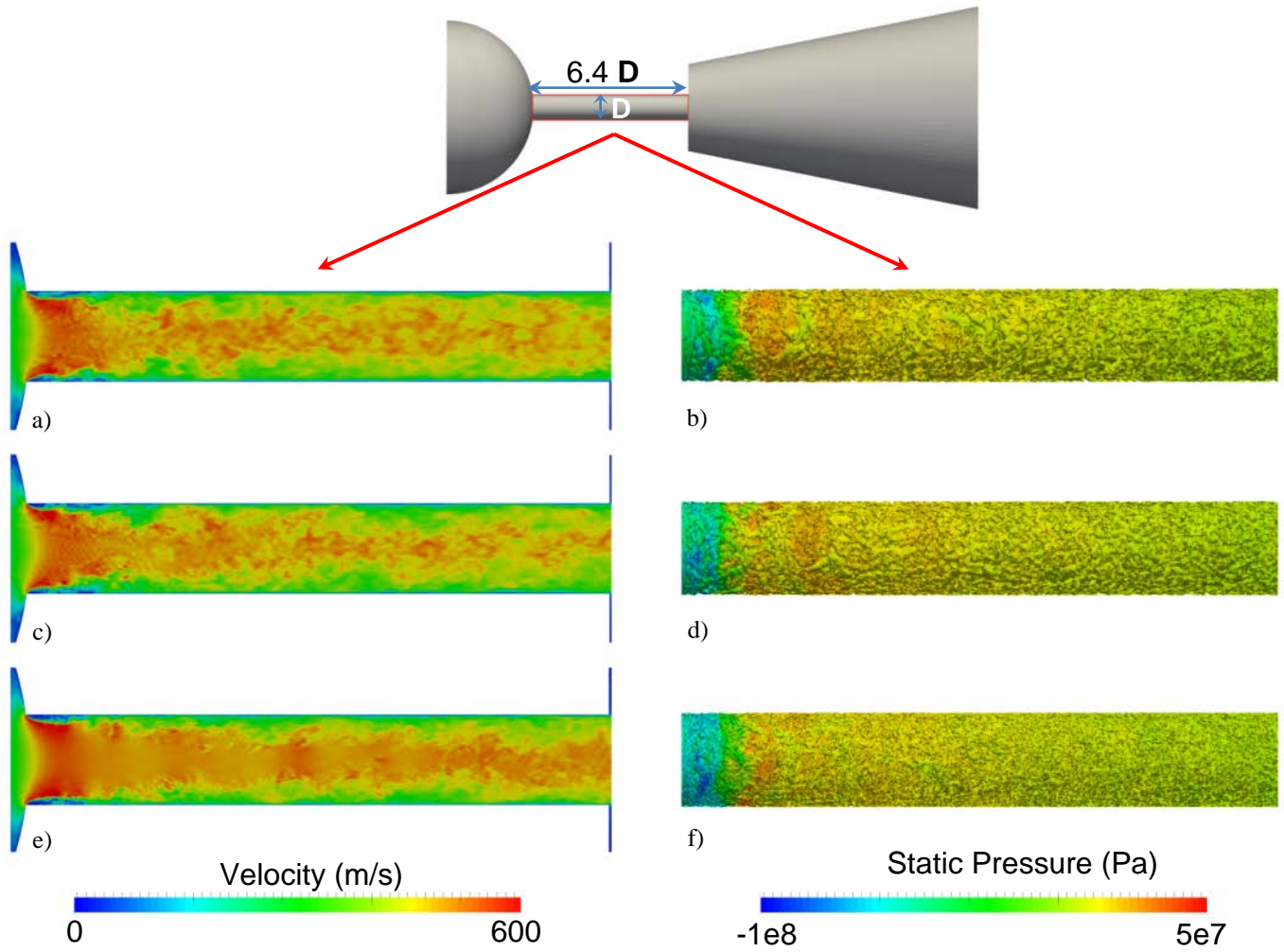
291   **Figure 4.** Jet liquid turbulent structures at quasi-steady stage (P_{inlet} = 1200 bar and Re = 37000 at the
292   orifice exit for coarse (a and b), medium (c and d) and fine (e and f) mesh cases. In the left column
293   (images a, c, and e), in-nozzle flow is coloured by velocity magnitude. In the right column at
294   corresponding times (images b, d, and f), the turbulent eddies are illustrated using a Q-criterion isosurface
295   of 5×10^9, coloured by static pressure. Negative static pressures after the nozzle entrance are due to the
296   absence of a cavitation model. Greater resolution of jet core and boundary layer turbulence are apparent
297   with increasing mesh density.

298   **3.2   Morphology of the penetrating jet**

299   Some instantaneous features such as flow structures and the evolution of spray transients are

300   presented in Figure 5 for three different mesh resolutions at 15 µs after start of penetration (ASOP)

301 showing the influence of mesh size on capturing surface instabilities. The umbrella-shaped leading edge

302 of the jet for coarse, medium, and fine cases shows a smooth surface with penetration velocity of 123 m/s

303 in agreement with DNS results [14, 34] for similar velocity ranges.

304 The irregularities on the trailing edge of the umbrella play a significant role in the disintegration

305 process of the penetrating jet. As can be seen in Figure 5, finer grids lead to capturing more waves

306 resulting in higher fragmentation rates.

307 Mesh resolution affects prediction of instabilities on the liquid jet behind the umbrella. In-nozzle-

308 generated turbulence in combination with relaxation of the velocity profile at the nozzle exit initiate the

309 perturbations leading to wave growth on the jet surface. As can be seen in Figure 5, surface instabilities

310 are triggered close to the nozzle orifice exit (further than one diameter for the fine grid) as a result of the

311 K-H mechanism (wave generation on jet surface based on aerodynamic interaction, creating ligaments

312 which then either disintegrate to produce droplets or just roll up and continue to develop).

a)

b)

c)

Velocity Magnitude (m/s)

313
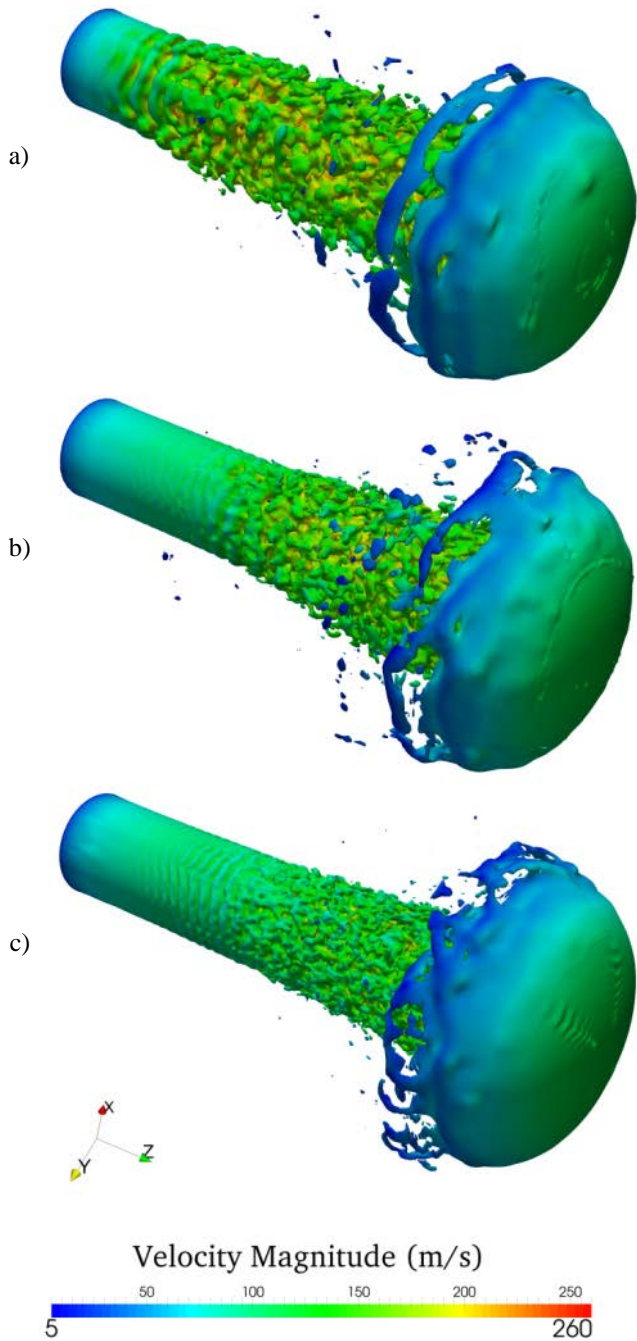
Figure 5. Structure of the jet colored by velocity magnitude at 15 µs ASOP, indicated by liquid interface of γ = 0.5, for coarse (a), medium (b) and fine (c) mesh cases showing over-prediction of breakup for the coarse case and the resolution of smaller scale surface instabilities and breakup for the finer case.

Inaccurate prediction of the velocity relaxation at the liquid-gas interface due to insufficient grid resolution intensifies the K-H mechanism, exaggerating the liquid jet disintegration process. Furthermore, the thickness of ligaments is a matter of the cell size where the pinching-off occurs as the thickness drops

18

320 below the cell size, followed by the generation of several droplets of varying sizes [8, 48, 49]. It can be

321 concluded that the mesh density at the air-fuel interface considerably influences the development of

322 ligaments and the breakup process.

323   Figure **6** shows a comparison of experimental images with the numerical results with the fine mesh

324 case at different times ASOP. Adding a 2× Barlow lens to the microscope to give a total magnification of

325 7.7:1 enables greater details of the early spray to be captured. The use of a dual frame CCD camera with a

326 time interval of one microsecond between subsequent images allows validation of the velocity of advance

327 of the leading edge and tracking of the transient changes in the morphology of the penetrating diesel jet.

Volume Fraction of Diesel Fuel

328
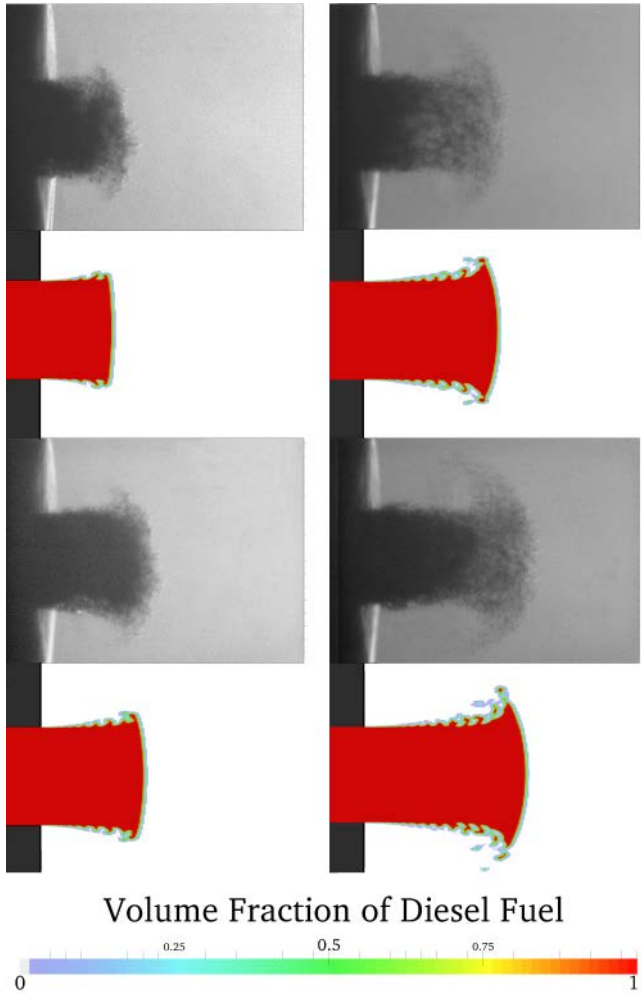
Figure 6. Comparison of experimental images with numerical results for the fine mesh case with highest magnification. Each experimental image is from a different injection event, apart from the first two (a and b) which are captured from two consecutive frames with 1 µs inter frame time.

Some transparency can be clearly seen in the shadowgraphy images. This is due to air inclusion within the liquid inside the orifice, left from previous injection. The existence of ingested air inside the injector was reported by Swantek et al. [46] at the end of injection (EOI) process. Air inclusion inside the injector influences the spray structure and could be a source of observed deviation between experimental and numerical results.

Shadowgraphy images are compared with the numerical results in Figure 7 with a larger field of view, presenting the general structure of the diesel spray. In this Figure, images *a* and *b*, *d* and *e*, *g* and *h*, *i* and *j* are paired, each pair is captured from the same injection event with one microsecond delay between consecutive frames.

The experimental images illustrate a more structured surface even very close to the nozzle exit compared with the numerical results. The leading edge of the emerging jet is disintegrating unlike the numerical results where the leading edge umbrella-shaped structure of the emerging jet is continuous liquid with breakup occurring more rapidly around the periphery. Air inclusion prior to start of injection could explain the rougher surface, and earlier disintegration of the leading edge in the experimental images resulting in the more oblique angle of the umbrella.

The necking of the jet length behind the umbrella can be obviously seen in the experimental images in Figure 7, while it is not as marked in the simulations. The difference is possibly related to the presence of air in the experimental jet, as indicated by partial transparency of the experimental images, and thus more rapid disintegration. The outer recirculating gas flow removes the generated droplets and advects them toward the outer flow which can be seen in images *i* and *j* of Figure 7.

a)

b)

c)

d)

e)

f)

g)

h)

i)

j)

t= 5 µs

t= 6 µs

t= 7µs

t= 8 µs

t= 9 µs

t= 10 µs

t= 11 µs

t= 12 µs

t= 13 µs

t= 14 µs

Volume Fraction of Diesel Fuel

0.25   0.5   0.75

0   1

21

352
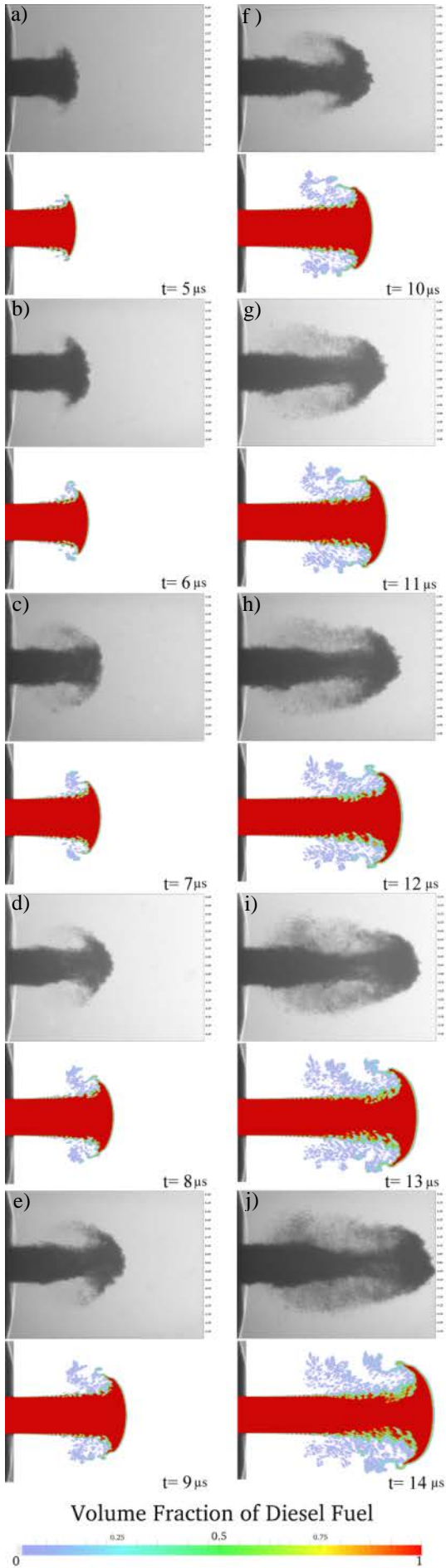
Figure 7. Comparison of experimental (with no magnification) and numerical results. Numerical results shown are for the fine mesh, colored by volume fraction of diesel fuel. Images a and b, d and e, g and h, i and j are paired, captured from the same injection event from two consecutive frames with 1 µs inter frame time.

Further differences between the experimental and numerical results are in the production of small droplets in the experimental images but not in the numerical results. This is due to the constraint in computational resources where the grid resolution in the computational domain is insufficient to resolve the small eddies in the air phase which influences the breakup processes of the ligaments and droplets.

Capturing two subsequent images enables velocity measurement of the jet leading edge. Experimental values for 100 double frame shots, with inter-frame times varying between 1 to 15 µs are shown in Figure 8. The error bars are based on the accuracy of the detection of the leading edge of the jet and this is a function of the inter-frame time. The jet penetration velocity at various axial distances from nozzle exit with corresponding time ASOP, demonstrated in Figure 8, show good agreement between numerical and experimental results. The Re is based on the average axial velocity at the nozzle exit.

Instantaneous mass flow rate was not measured. Quasi-steady mass flow rate was measured at 0.0139 kg/s and numerically predicted at 0.0168 kg/s. The difference is assumed to be due primarily to the absence of cavitation in the simulations.
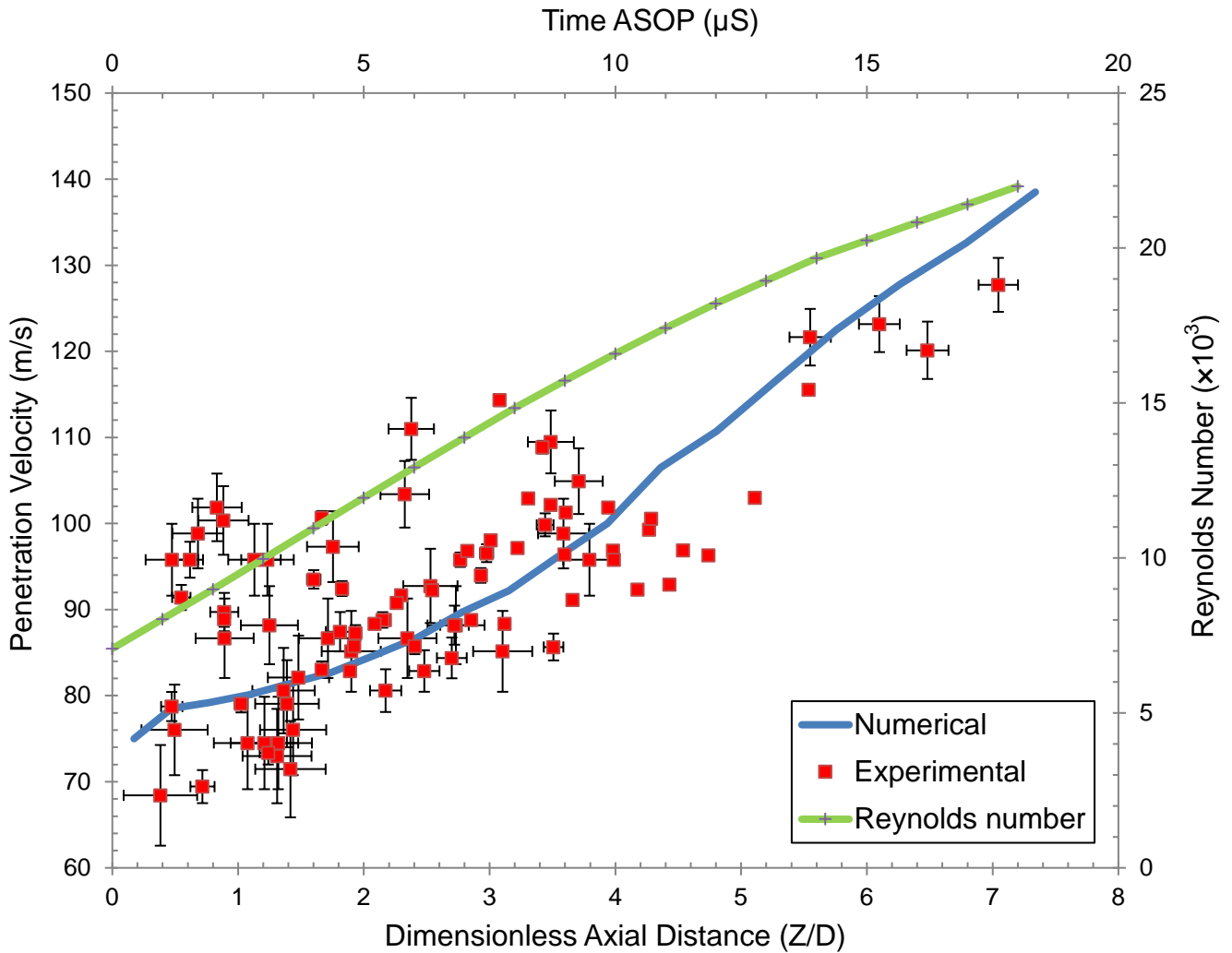
Figure 8. Comparison of measured and predicted jet penetration velocity at various axial distances from nozzle exit with corresponding times ASOP. Re values, from computation, are calculated using the average velocity of liquid at the nozzle exit.

3.3 Numerical schemes

The behavior of different interpolation schemes is presented in Figure 9, Figure 10, and Figure 11

The order of the temporal integration schemes for phase-fraction and governing conservation equations

plays a significant role in prediction of small-scale eddies inside the nozzle orifice. As depicted in Figure

9, at the quasi-steady stage, employing the second-order scheme named *Backward* results in smaller scale

eddies in comparison to the first-order, *Euler*, approach due to higher dissipation in the first-order

scheme. This influences irregularities which are mainly generated by the reduction of the cross-sectional

381 area at the nozzle inlet where there is strong change in flow direction, and vena contracta phenomena

382 [50].
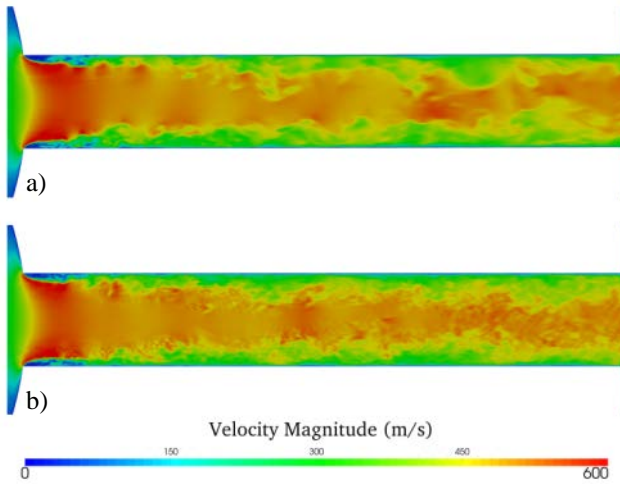
Figure 9. Influence of the time derivative order on prediction of turbulent structures within the nozzle orifice at quasi-steady stage (P_{inlet} = 1200 bar), colored by velocity magnitude, for the fine grid case with; a) Euler, first-order and b) Backward, second-order.

The first-order discrete equations are more diffusive than the second-order discrete equations [41].The impact of the time interpolation method is also seen in Figure 10, at 14 µs ASOP. The disintegration of droplets from the liquid jet surface behind the leading edge diminishes with the first-order scheme compared with the second-order scheme. The second-order accurate interpolation scheme enables modelling of smaller fluctuations of velocity in the liquid-gas interface. Therefore, the K-H waves intensify behind the umbrella-shaped leading edge resulting in higher rates of separation. This separation narrows the liquid jet, demonstrating the necking phenomena of the spray. This necking process is weakened in the first-order interpolation scheme due to higher dissipation (in-efficiency in resolving smaller eddies) in this method. This is why the second-order scheme for time derivatives has been employed for the present study.
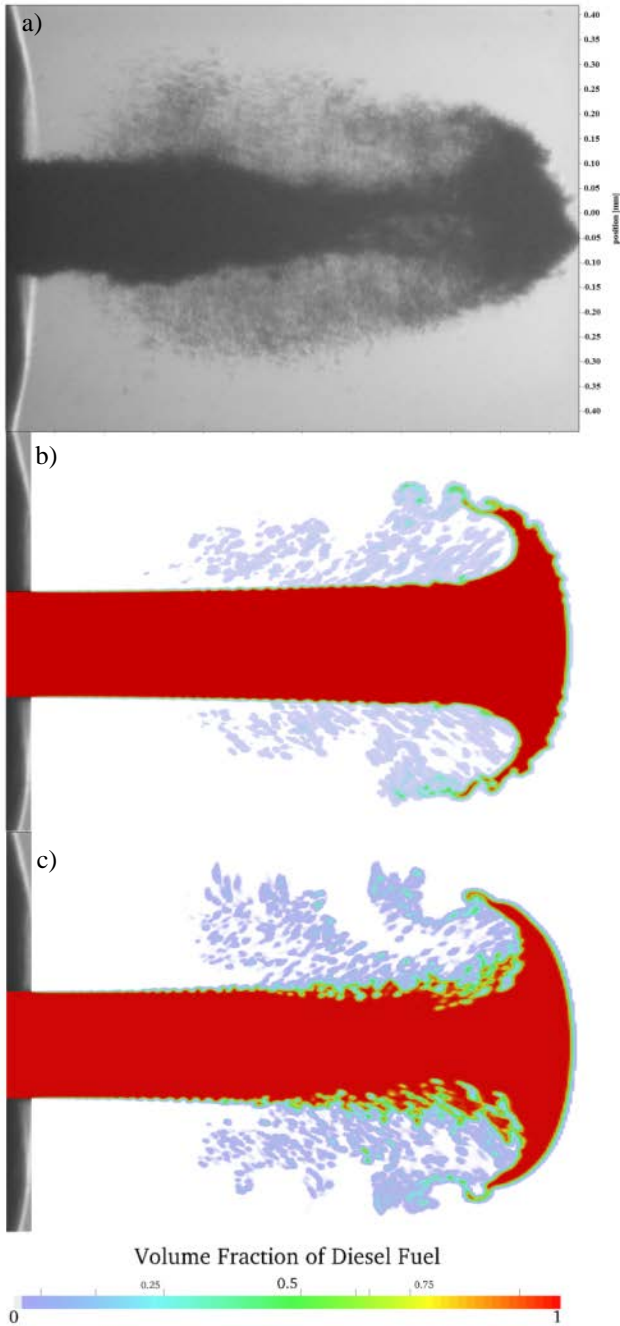
Figure 10. Comparison of an experimental image with numerical results showing the effect of the order of temporal integration scheme on the jet disintegration process at t = 14 μs ASOP, colored by volume fraction of diesel fuel, for the fine resolution case; a) Experiment, b) First-order, and c) Second-order.

The influence of the convection-specific interpolation scheme on capturing the liquid-gas interface is illustrated qualitatively in **Figure 11** for medium grid resolution. Different ranges of first/second order bounded numerical schemes have been investigated from the more dissipative, Total Variation Diminishing (TVD), up to the more conservative NV schemes. The NV Gamma scheme showed a

25

smooth leading edge surface which is in agreement with DNS results of [14, 34] at a similar penetration velocity. Thus, the NV Gamma scheme has been selected for solving the convection terms. The presence of air in the liquid could play a role in the generation of surface roughness in the leading edge of the experimental jet which is not seen in the simulations.

Secondary interfacial instabilities known as Rayleigh-Taylor (R-T) instabilities may develop when the propagation velocity is sufficient to exceed a critical value. If R-T instability develops, it presents as a rapid crosswise modulation on the leading edge followed by shedding of drops [11]. These interfacial instabilities grow as the jet proceeds downstream and increase gas penetration into the core liquid. The latter forms 'blobs' joined by thin core ligaments. These blobs finally snap and complete the core breakup process. The simulations capture an umbrella-shaped leading edge which qualitatively is in agreement with the experimental results as shown in Figure 6 and Figure **7**, although no spanwise instabilities due to the R-T mechanism are apparent with the NV Gamma scheme. Figure 11 demonstrates that certain convection interpolation schemes may give apparent or Rayleigh-Taylor (R-T)-like instabilities which are not necessarily physical.
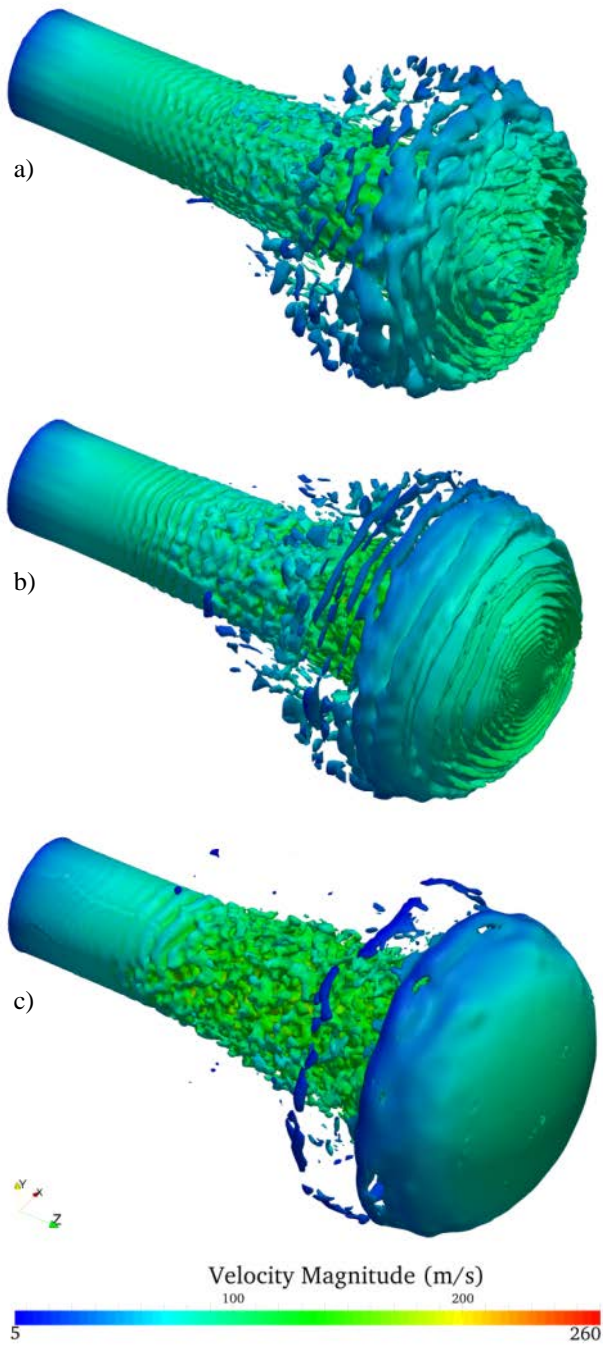
**Figure 11.** The effect of convection-specific interpolation schemes on capturing surface instabilities of the jet beyond the nozzle exit for the medium resolution grid at t = 14 µs ASOP, indicated by volume fraction of γ = 0.5, and colored by velocity magnitude; a) TVD, FilteredLinear, b) TVD, LimitedLinear, and c) NV, Gamma

## 3.4   Spray structure of diesel fuel at quasi-steady operating condition (pressure = 1200 bar)

The atomized liquid fraction on the spray surface for the three mesh resolutions is illustrated in Figure 12 by γ = 0.1 isosurfaces, coloured by the velocity magnitude at the quasi-steady stage where

427 diesel fuel pressure at sac inlet is 1200 bar. The onset of primary atomization can be seen close to the

428 nozzle exit for the three mesh resolutions. Very fine droplets are captured near the nozzle exit noticeably

429 in the finest case (20 million cells) which agrees with the experimental images. The surface velocity

430 decelerates rapidly close to the orifice exit due to relaxation of the velocity profile. The number of

431 discrete droplets captured for the coarse, medium and fine meshes at the quasi-steady stage are 4830,

432 9494, and 22076 respectively. The increase in apparent atomization from finer meshes is due to better

433 prediction of the smaller-scale in-nozzle turbulent structures as presented in Figure 4, resulting in smaller-

434 scale surface eddies which intensify the breakup process. Consequently, the breakup rate increases in

435 cases with higher mesh resolution. The atomization rate at the quasi steady stage is 0.0139, 0.0148, and

436 0.0158 kg/s for coarse, medium and fine mesh, respectively. The finer the mesh, the finer the resolved

437 droplets. Mesh independence is not demonstrated due to limited computer resources and unfeasible

438 computation time.
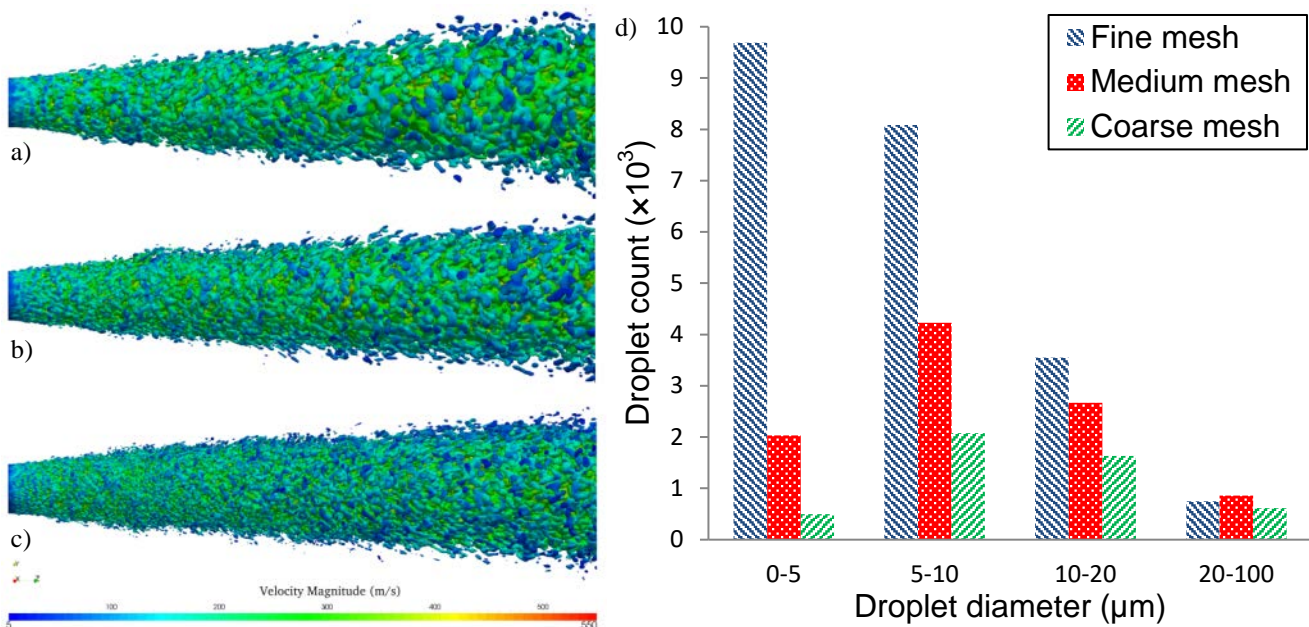
Figure 12. Spray morphology within 12 nozzle diameters of the nozzle exit, indicated by isosurface of volume fraction $\gamma = 0.1$, colored by velocity magnitude at quasi-steady stage ($P_{inlet} = 1200$ bar); a) Coarse, b) Medium and c) Fine case showing decreasing scale of surface features with increasing mesh resolution. Panel d) shows quantitatively the greater number of fine droplets generated with finer meshes.

444   Figure 13 illustrates a close-up view of the jet disintegration, visualized using the isosurface of

445      $\gamma = 0.5$ for the fine mesh case, at the quasi-steady stage. This picture represents the jet surface detachment

446   and droplet generation, occurring even at one nozzle diameter downstream.

447
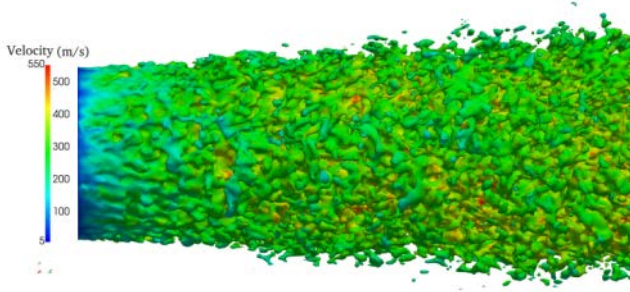
Figure 13. Close-up view showing the onset of surface breakup visualized by isosurface of $\gamma = 0.5$
colored by velocity for the fine mesh case at quasi-steady stage (P_{inlet} = 1200 bar).

450   The growth of non-axisymmetric disintegration at different cross-sections from the nozzle exit is

451   presented in Figure 14. The formation of small longitudinal waves can be seen at one nozzle diameter

452   downstream of the nozzle exit. At one diameter downstream primary breakup is triggered and intensifies

453   farther downstream. Up to 5 diameters from nozzle exit, the core breakup process is fully developed since

454   the liquid core is narrowing to tapered ligaments. The liquid core is totally disintegrated at 8 diameters

455   downstream, resulting in higher numbers of droplets than at the positions upstream.
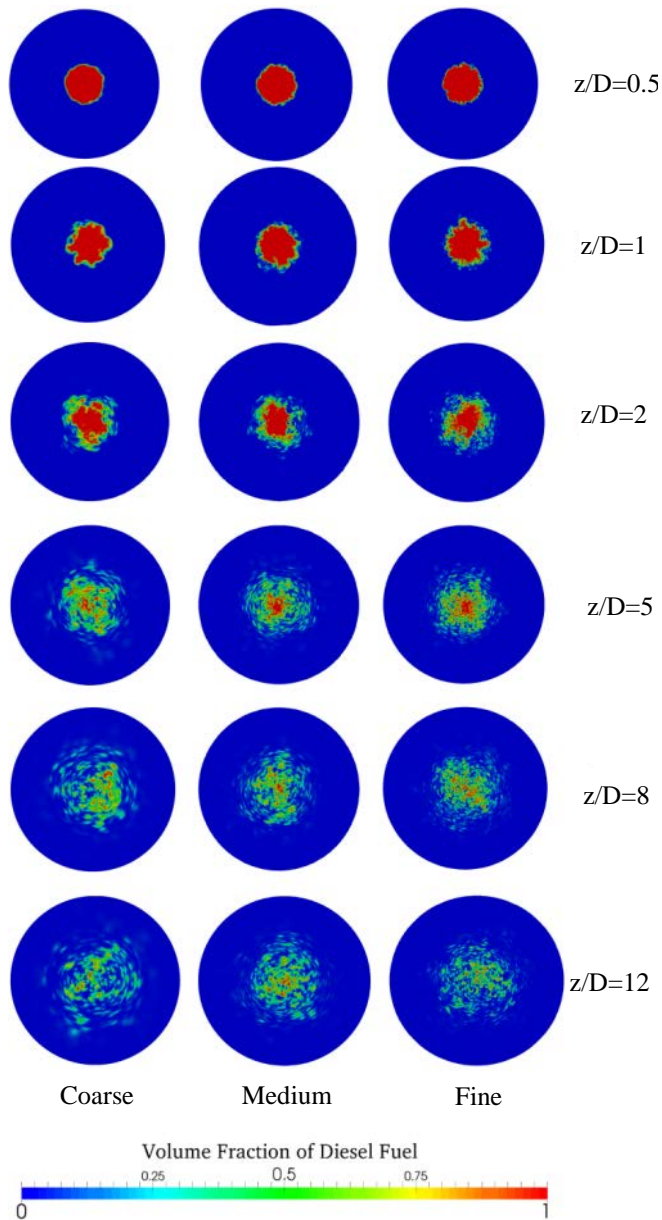
Figure 14. Liquid distribution in cross-sectional planes at different streamwise positions downstream of the nozzle exit for the coarse (left column), medium (middle column) and fine (right column) cases at quasi-steady stage (P_{inlet} = 1200 bar).). The value of z/D indicates the number of nozzle diameters downstream of the nozzle exit.

Figure 15 illustrates the liquid core visualized using the $\gamma = 0.95$ isosurface at quasi-steady stage (P_{inlet} = 1200 bar) for different meshes. It can be seen that longitudinal surface perturbations develop near the nozzle exit. The liquid core tapers progressively before disintegrating into large clusters which is in accordance with the limited available data by [51]. The fine mesh case shows an extended liquid core

30

compared to the coarser cases. This is due to pinching-off of smaller droplets from thinner ligaments detached from the liquid jet surface which slows down the liquid core disintegration process [8, 48, 49].
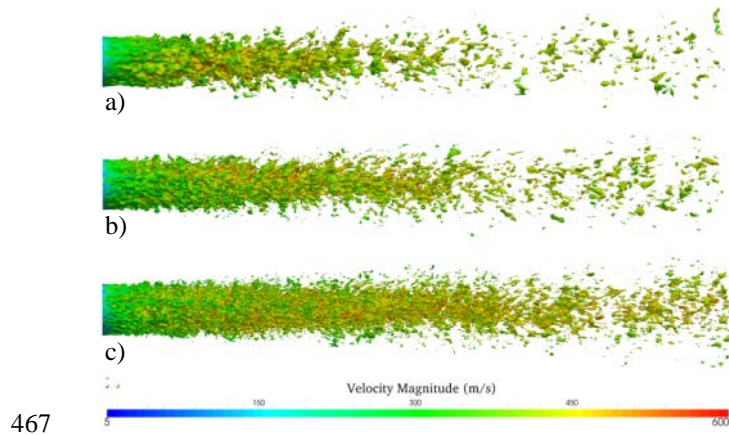
Figure 15. Effect of mesh resolution on jet liquid core length depicted by $\gamma= 0.95$ isosurface for a) Coarse, b) Medium and c) Fine mesh cases at quasi-steady stage ($P_{inlet} = 1200$ bar).

Figure 16 depicts the early spray angle (ϕ) at quasi-steady stage, measured on a spray image using edge detection based on a threshold filter. The formation and development of shear layer instabilities can be clearly seen. The nozzle tip is apparent on the left side of the image.
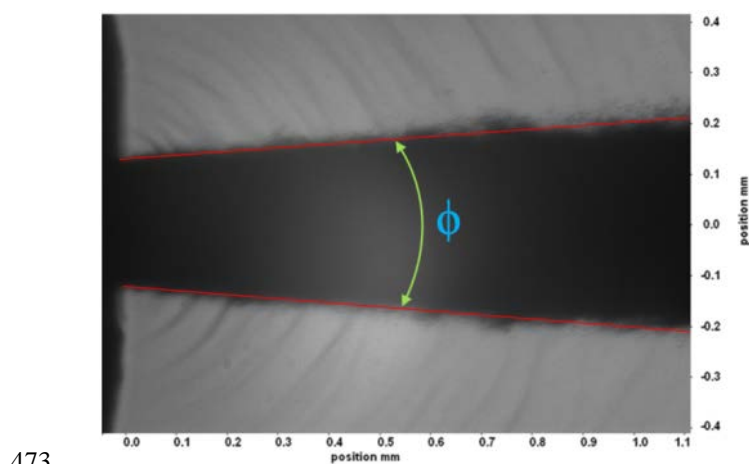

Figure 16. Shadowgraphy of the diesel nozzle spray at quasi-steady stage ($P_{inlet} = 1200$ bar), using long distance microscope[45].

To compare the predicted numerical early spray angle with experiment, Leboissetier & Zaleski [52] core analysis was conducted. Based on this method, three different zones in the numerical data were

distinguished at every time step during the quasi-steady stage. The results of this analysis for three different cases are depicted in Figure 17, showing the time-averaged structure of the atomization region. The red zone contains only liquid (never contains gas), thus representing the liquid core; the blue region is gas only while the green region contains sporadic liquid and gas volumes depicting the atomization zone. The early spray angle was extracted using the outer boundary of the two phase mixture (green) zone.
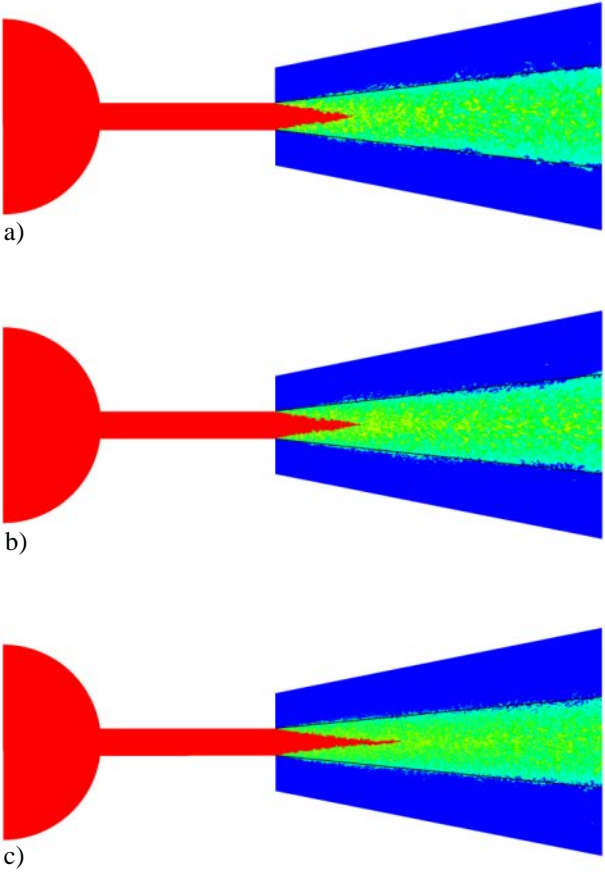
Figure 17. A Leboissetier & Zaleski [52] core analysis for, a) Corase, b) Medium, and c) Fine at quasi-steady stage, P_{inlet}=1200 bar; red and blue region experienced only liquid and gas, respectively. The green zone is the atomization region.

A summary of this investigation, gathered using these plots (Figure 17) is tabulated in Table 4, showing the reduction in spray angle and increase in liquid core length for the higher mesh resolution cases. For comparison, the core length predicted by Hiroyasu and Arai's correlation [17] is also shown.

491 The predicted core length appears to be too small and this may be partly due to the methods used to

492 determine core length and partly due to the absence of a cavitation model, and thus overly high jet

493 turbulence.

494 **Table 4.** Comparison of spray angle and liquid core length

Case	Early Spray Angle	Core Length (mm)
Experiment	$8.7 \pm 0.4°$	-
Coarse	$13.22 \pm 1°$	0.71 ± 0.05
Medium	$12.52 \pm 0.8°$	0.73 ± 0.05
Fine	$11.26 \pm 0.5°$	1.151 ± 0.02
Hiroyasu & Arai [17]		9.13

495 ## 4. Conclusions

496 The general structure of primary atomization of diesel sprays was successfully characterized

497 numerically employing an Eulerian/LES/VOF approach to capture free surfaces. The umbrella-shaped

498 leading edge of the emerging jet was captured successfully near the nozzle exit. The experimental

499 shadowgraphy images showed a rougher surface, greater transparency, more oblique angle and earlier

500 disintegration of the leading edge in comparison with the numerical prediction. This is presumed due to

501 in-nozzle air inclusions left from the previous injection event. The necking of the liquid jet behind the

502 umbrella-shaped leading edge is captured in both experimental and numerical results. The temporal

503 variation of jet penetration velocity and Reynolds number show favorable agreement between numerical

504 and experimental results. The second-order temporal integration scheme and NV Gamma convection-

505 specific interpolation scheme resulted in a better prediction of small scale eddies and jet surface structures

506 compared with the first-order integration scheme and TVD convection-specific interpolation schemes.

507 A mesh resolution study for the two stages of the spray, initial penetration and quasi-steady, revealed

508 that:

- fragmentation of the jet commenced close to nozzle exit (within about one diameter from exit) for the finest mesh

- modelling of the primary breakup process is enhanced with higher mesh resolution

- droplet sizes decrease with increasing mesh resolution

- smaller eddies were captured with decreasing cell size inside the nozzle

- increasing mesh resolution leads to decrease in the early spray angle and increase in the liquid core length, leading to better agreement between experiment and numerical predictions.

Acknowledgments

References

[1] S. Moon, Y. Gao, S. Park, J. Wang, N. Kurimoto, Y. Nishijima, Effect of the number and position of nozzle holes on in-and near-nozzle dynamic characteristics of diesel injection, Fuel, 150 (2015) 112-122.

[2] Y. Wang, L. Qiu, R.D. Reitz, R. Diwakar, Simulating cavitating liquid jets using a compressible and equilibrium two-phase flow solver, International Journal of Multiphase Flow, 63 (2014) 52-67.

[3] S. Moon, Y. Gao, J. Wang, K. Fezzaa, T. Tsujimura, Near-field dynamics of high-speed diesel sprays: Effects of orifice inlet geometry and injection pressure, Fuel, 133 (2014) 299-309.

[4] F. Coletti, M.J. Benson, A.L. Sagues, B.H. Miller, R. Fahrig, J.K. Eaton, Three-Dimensional Mass Fraction Distribution of a Spray Measured by X-Ray Computed Tomography, Journal of Engineering for Gas Turbines and Power, 136 (2014) 051508.

[5] V. Vuorinen, J. Yu, S. Tirunagari, O. Kaario, M. Larmi, C. Duwig, B.J. Boersma, Large-eddy simulation of highly underexpanded transient gas jets, Physics of Fluids (1994-present), 25 (2013) 016101.

[6] O. Kaario, V. Vuorinen, T. Hulkkonen, K. Keskinen, M. Nuutinen, M. Larmi, F.X. Tanner, Large Eddy Simulation of High Gas Density Effects in Fuel Sprays, Atomization and Sprays, 23 (2013).

[7] H. Großhans, Large Eddy Simulation of Atomizing Sprays, in, Lund University, 2013, pp. 115.

[8] M. Gorokhovski, M. Herrmann, Modeling primary atomization, Annu. Rev. Fluid Mech., 40 (2008) 343-366.

[9] C.H. Bong, Numerical and experimental analysis of diesel spray dynamics including the effects of fuel viscosity, in: Australian Maritime College, University of Tasmania, 2010.

[10] R. Gjesing, J.H. Hattel, U. Fritsching, Coupled atomization and spray modelling in the spray forming process using openfoam, Engineering Applications of Computational Fluid Mechanics, 3 (2009) 471-486.

[11] E. De Villiers, A.D. Gosman, H.G. Weller, Large eddy simulation of primary diesel spray atomization, SAE transactions, 113 (2004) 193-206.

[12] V. Vuorinen, M. Larmi, P. Schlatter, L. Fuchs, B.J. Boersma, A low-dissipative, scale-selective discretization scheme for the Navier–Stokes equations, Computers & Fluids, 70 (2012) 195-205.

[13] V. Vuorinen, H. Hillamo, O. Kaario, M. Larmi, L. Fuchs, Large Eddy Simulation of droplet stokes number effects on turbulent spray shape, Atomization and Sprays, 20 (2010).

[14] J. Shinjo, A. Umemura, Detailed simulation of primary atomization mechanisms in Diesel jet sprays (isolated identification of liquid jet tip effects), Proceedings of the Combustion Institute, 33 (2011) 2089-2097.

[15] Y.J. Wang, K.S. Im, K. Fezzaa, W.K. Lee, J. Wang, P. Micheli, C. Laub, Quantitative x-ray phase-contrast imaging of air-assisted water sprays with high Weber numbers, Applied physics letters, 89 (2006) 151913.

[16] M. Stahl, M. Gnirß, N. Damaschke, C. Tropea, Laser Doppler measurements of nozzle flow and optical characterisation of the generated spray, in: ILASS, Orleans, France, 2005.

[17] H. Hiroyasu, M. Arai, Structures of fuel sprays in diesel engines, in, SAE Technical Paper, 1990.

[18] L. Bravo, C. Ivey, D. Kim, S. Bose, High-fidelity simulation of atomization in diesel engine sprays, in: Proceedings of the Summer Program, 2014, pp. 89.

[19] C. Baumgarten, Mixture formation in internal combustion engines, Springer, Germany, 2006.

[20] M. Herrmann, On simulating primary atomization using the refined level set grid method, Atomization and Sprays, 21 (2011) 283-301.

[21] G.M. Faeth, L.P. Hsiang, P.K. Wu, Structure and breakup properties of sprays, International Journal of Multiphase Flow, 21 (1995) 99-127.

[22] P.K. Wu, G.M. Faeth, Aerodynamic effects on primary breakup of turbulent liquids, Atomization and Sprays, 3 (1993).

[23] P.K. Wu, L.K. Tseng, G.M. Faeth, Primary breakup in gas/liquid mixing layers for turbulent liquids, Atomization and Sprays, 2 (1992).

[24] R. Domann, Y. Hardalupas, Breakup model for accelerating liquid jets, in: Proceedings of 42nd AIAA Aerospace Science Meeting and Exhibition, 2004.

[25] C. Badock, R. Wirth, A. Fath, A. Leipertz, Investigation of cavitation in real size diesel injection nozzles, International Journal of Heat and Fluid Flow, 20 (1999) 538-544.

[26] C. Arcoumanis, H. Flora, M. Gavaises, M. Badami, Cavitation in real-size multi-hole diesel injector nozzles, SAE Trans., J. Engines, 109 (2000) 3.

[27] H. Chaves, C.H. Ludwig, Characterization of cavitation in transparent nozzles depending on the nozzle geometry, in: Proc. Annu. Conf. Inst. Liq. Atom. Spray Syst., 18th (ILASS-2005), Orleans, France, 2005, pp. 259-264.

[28] M. Stahl, N. Damaschke, C. Tropea, Experimental investigation of turbulence and cavitation inside a pressure atomizer and optical characterization of the generated spray, in: Proceedings of international conference on liquid atomization and spray systems, 10th ICLASS, Kyoto, Japan, Paper, 2006.

[29] C.M. Varga, J.C. Lasheras, E.J. Hopfinger, Initial breakup of a small-diameter liquid jet by a high-speed gas stream, Journal of Fluid Mechanics, 497 (2003) 405-434.

[30] K.A. Sallam, Z. Dai, G.M. Faeth, Liquid breakup at the surface of turbulent round liquid jets in still gases, International Journal of Multiphase Flow, 28 (2002) 427-449.

[31] M. Linne, M. Paciaroni, T. Hall, T. Parker, Ballistic imaging of the near field in a diesel spray, Experiments in fluids, 40 (2006) 836-846.

[32] X. Jiang, G.A. Siamas, K. Jagus, T.G. Karayiannis, Physical modelling and advanced simulations of gas–liquid two-phase jet flows in atomization and sprays, Progress in Energy and Combustion Science, 36 (2010) 131-167.

[33] V. Vuorinen, H. Hillamo, O. Kaario, M. Nuutinen, M. Larmi, L. Fuchs, Effect of droplet size and atomization on spray formation: A priori study using large-eddy simulation, Flow, turbulence and combustion, 86 (2011) 533-561.

[34] J. Shinjo, A. Umemura, Simulation of liquid jet primary breakup: Dynamics of ligament and droplet formation, International Journal of Multiphase Flow, 36 (2010) 513-532.

[35] O. Desjardins, V. Moureau, H. Pitsch, An accurate conservative level set/ghost fluid method for simulating turbulent atomization, Journal of Computational Physics, 227 (2008) 8395-8416.

[36] O. Desjardins, H. Pitsch, Detailed numerical investigation of turbulent atomization of liquid jets, Atomization and Sprays, 20 (2010).

[37] A. Yoshizawa, K. Horiuti, A statistically-derived subgrid-scale kinetic energy model for the large-eddy simulation of turbulent flows, Journal of the Physical Society of Japan, 54 (1985) 2834-2839.

[38] H.G. Weller, A new approach to VOF-based interface capturing methods for incompressible and compressible flow, OpenCFD Ltd., Report TR/HGW/04, (2008).

[39] R.I. Issa, Solution of the implicitly discretised fluid flow equations by operator-splitting, Journal of Computational Physics, 62 (1986) 40-65.

[40] B. Befrui, A. Aye, P. Spiekermann, D.L. Varble, M.A. Shost, M.C. Lai, J. Wang, GDi Skew-Angled Nozzle Flow and Near-Field Spray Analysis using Optical and X-Ray Imaging and VOF-LES Computational Fluid Dynamics, in, SAE Technical Paper, 2013.

[41] H. Jasak, Error analysis and estimation for the finite volume method with applications to fluid flows, (1996).

[42] N. Papadopoulos, P. Aleiferis, Numerical Modelling of the In-Nozzle Flow of a Diesel Injector with Moving Needle during and after the End of a Full Injection Event, SAE International Journal of Engines, 8 (2015) 2285-2302.

[43] M. Battistoni, C. Poggiani, S. Som, Prediction of the Nozzle Flow and Jet Characteristics at Start and End of Injection: Transient Behaviors, SAE International Journal of Engines, 9 (2015).

[44] M. Battistoni, Q. Xue, S. Som, E. Pomraning, Effect of Off-Axis Needle Motion on Internal Nozzle and Near Exit Flow in a Multi-Hole Diesel Injector, SAE International Journal of Fuels and Lubricants, 7 (2014) 167-182.

[45] L. Goldsworthy, C.H. Bong, P.A. Brandner, Measurements of diesel spray dynamics and the influence of fuel viscosity using PIV and shadowgraphy, Atomization and Sprays, 21 (2011).

[46] A.B. Swantek, D. Duke, F.Z. Tilocco, N. Sovis, C.F. Powell, A.L. Kastengren, End of Injection, Mass Expulsion Behaviors in Single Hole Diesel Fuel Injectors, in: ILASS Americas 26th Annual Conference on Liquid Atomization and Spray Systems, Portland, OR, USA, 2014.

[47] H. Jasak, H.G. Weller, A.D. Gosman, High resolution NVD differencing scheme for arbitrarily unstructured meshes, International journal for numerical methods in fluids, 31 (1999) 431-449.

[48] D. Kim, O. Desjardins, M. Herrmann, P. Moin, Toward two-phase simulation of the primary breakup of a round liquid jet by a coaxial flow of gas, Center for Turbulence Research Annual Research Briefs, 185 (2006).

[49] D. Kim, O. Desjardins, M. Herrmann, P. Moin, The primary breakup of a round liquid jet by a coaxial flow of gas, in: ILASS Americas 20th Annual Conference on Liquid Atomization and Spray Systems, 2007.

[50] R. Payri, J.M. Garcia, F.J. Salvador, J. Gimeno, Using spray momentum flux measurements to understand the influence of diesel nozzle geometry on spray characteristics, Fuel, 84 (2005) 551-561.

[51] A. Fath, C. Fettes, A. Leipertz, Investigation of the Diesel Spray Break-Up Close to the nozzle at different Injection conditions, in: Fourth International Symposium on Diagnostics and Modeling of Combustion in Internal Combustion Engines, Kyoto, Japan, JSME, 1998, pp. 429-434.

[52] A. Leboissetier, S. Zaleski, Direct numerical simulation of the atomization of a liquid jet, in: Proceeding of the ILASS-Europe, 2001, pp. 2-6.